



Can isothermal plane Couette flow in fluid overlying porous layer be linearly unstable?

N. Barman¹, A. Aleria¹ and P. Bera^{1,†}

¹Department of Mathematics, Indian Institute of Technology Roorkee, Roorkee 247667, India

(Received 9 March 2024; revised 26 August 2024; accepted 26 September 2024)

The present study aims to examine the temporal linear stability analysis of isothermal plane Couette flow over a porous layer using the two-domain approach. The flow in the porous layer is described by the unsteady Darcy–Brinkman equations, whereas it is characterised by the Navier–Stokes equations in the fluid layer. In contrast to the Darcy model, it is observed that the isothermal plane Couette flow becomes unstable for such a superposed system on the inclusion of the Brinkman term. From the stability analysis, the two-dimensional mode is found to be least stable, and two modes of instability, namely porous mode and mixed mode are obtained under the consideration of the Darcy–Brinkman model along with advection term (DBA model). For Darcy number (δ) = 0.01, depending on the value of the stress-jump coefficient, mixed mode controls the instability of the system at small values of depth ratio (\hat{d}), and it disappears for relatively high values of \hat{d} , where the porous mode dominates. In addition, it has been observed that when $\hat{d} = 0.1$, the critical mode of instability is found to be mixed for $\delta > 0.02$ and porous for $\delta \leq 0.02$. The stress-jump coefficient destabilises the flow in terms of energy production through perturbed stresses at the interface. As observed in the case of isothermal plane Poiseuille flow studied by Chang, Chen & Straughan (*J. Fluid Mech.*, vol. 564, 2006, pp. 287–303), here also depth ratio (Darcy number) stabilises (destabilises) the flow. However, this characteristic does not remain valid when the advection term is eliminated from the considered momentum equation. For a certain range of $\hat{d}(\delta)$, the destabilising (stabilising) characteristic of the respective parameters are encountered when the fluid mode of instability prevails.

Key words: shear-flow instability, porous media, multiphase flow

† Email address for correspondence: pberafma@iitr.ac.in

1. Introduction

Understanding and exploring the scenarios concerning the instability in one of Navier–Stokes (NS) equations' simplest non-trivial solution, i.e. plane Couette flow, is long overdue amidst the fluid mechanics community. Rayleigh (1914) first suggested the stable nature of plane Couette flow to infinitesimal disturbances in a channel. The first scientific proof to the preceding fact was given by Davey (1973). He used a combination of asymptotic analysis and numerical computation to prove the same. Later on, Romanov (1973) showed that Couette flow in the channel is stable for all Reynolds numbers using the linear stability analysis. This result was further supported by Orszag & Patera (1980). However, Tillmark & Alfredsson (1992) executed the first flow visualisation for transition in plane Couette flow experimentally and determined the critical Reynolds number for turbulence as 360 ± 10 based on the half-height of the channel and half-velocity difference between the walls. Such contrasting results between theoretical and experimental studies led several researchers to look for possible instability in plane Couette flow in a channel. Furthermore, wherein the researchers were still finding the Couette flow to be linearly stable (Lee & Finlayson 1986), following Nield (2003), Shankar, Shivakumara & Kumar (2020) predicted the hydrodynamic instability of plane Couette flow in a channel filled with the porous medium by including the Brinkman as well as advection term in Darcy model.

The study of fluid flow through a channel in which the fluid layer overlies the porous layer has garnered considerable attention from the scientific world in the late 20th century in view of its immense applications in various geological and industrial frameworks. We quote a few notable results: water flow below the surface of the Earth (Ewings & Weekes 1998), the oil flow in subterranean reservoirs (Allen 1984) and the production of composite materials for the automobile and aircraft industries (Blest *et al.* 1999). In particular, the interplay between the injected fluid and the porous layers is very important in enhanced oil recovery techniques, such as gas injection and water flooding. Stability analysis in this context provides valuable insight into the flow dynamics, enabling engineers to determine the optimal injection rates and pressure. By analysing the stability of the flow, one can predict and address instabilities such as channelling or fingering, which can lead to inefficient displacement of oil. This ensures that the injected fluid displaces the oil uniformly and effectively, thereby maximising recovery efficiency. Furthermore, vessel dynamics in marine engineering requires a sound understanding of the Couette flow in fluid overlying porous layer to optimise the interaction between fluid flow and a vessel's structure (Gourlay 2006; Wang *et al.* 2018; Mukherjee & Giribabu 2021). This interaction can significantly affect performance, efficiency and safety by notably influencing drag through the water and the porous coating on a ship's hull. Along these lines, a theoretical understanding of Couette flow in fluid overlying porous layer will be beneficial and, consequently, in the present study, an attempt has been made in this direction.

As can be seen in literature, the isothermal plane Couette flow is linearly stable to infinitesimal disturbances under Darcy's law (Chang, Chen & Chang 2017). Even the inclusion of media anisotropy and inhomogeneity fails to render instability in this situation (Barman, Aleria & Bera 2024). In contrast to the linearly unstable nature of Newtonian fluid (Chang, Chen & Straughan 2006; Chang *et al.* 2017), the isothermal plane Poiseuille/Couette–Poiseuille flow in fluid overlying porous layer is linearly stable for a Bingham fluid (Sengupta & De 2019, 2020). However, using non-modal analysis, the instability characteristic of the flow has been analysed in such a superposed system. The instability in plane Couette flow in fluid overlying porous layer was first witnessed by Chang (2005), in which the author considered a constant temperature difference between

Isothermal plane Couette flow over a porous layer

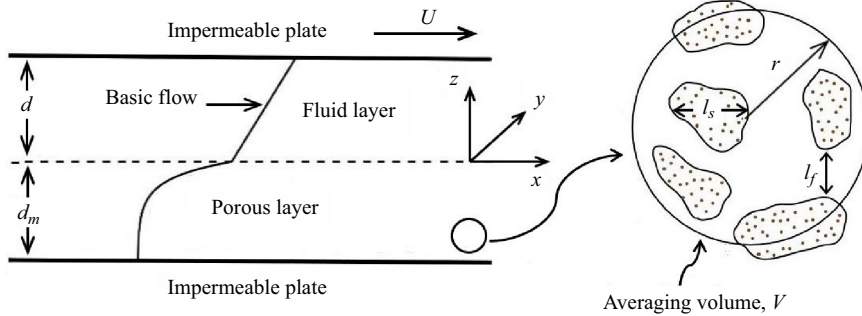


Figure 1. Diagram of the physical problem.

the upper and lower plate, and recent developments in this direction are well-documented in the recent article of Barman *et al.* (2024). To the best of the authors' knowledge, no literature exists that predicts the existence of instability in isothermal plane Couette flow through fluid overlying porous layer. Thus, the question that arises from the literature so far is whether it is possible to have a situation in which one can encounter the instability of isothermal plane Couette flow in the fluid overlying the porous layer. Answering this serves as the main objective of the present study.

The article advances as follows. Section 2 comprises the problem geometry and the governing equations, which is followed by exploring the neutral stability curves for possible existence of instability in § 3. It also reveals the physical cause behind the instability through the energy analysis and secondary flow patterns. The article ends with some concluding remarks in § 4.

2. Physical problem and mathematical formulation

2.1. Governing equations and boundary conditions

Consider a three-dimensional Couette flow in a horizontal fluid layer underlying a homogeneous and isotropic porous layer saturated with the same viscous, Newtonian and incompressible fluid (see figure 1). We assume that the physical properties of the fluid, namely, the density and dynamic viscosity, and the porous media properties, namely, the porosity and media permeability, are constant. Consider a Cartesian coordinate system (x, y, z) with the origin at the fluid–porous interface, wherein x , y and z signify the streamwise, spanwise and cross-stream flow directions, respectively. The depth of the fluid and porous layers are d and d_m , respectively. The upper plate of the fluid layer moves with a uniform velocity U in the streamwise direction, and the occupying space of the flow is $\{(x, y, z) \in \mathbb{R}^2 \times (-d_m, d)\}$. A two-domain approach has been chosen to understand the role of location of the interface on the stability of the above shear-induced flow.

The flow in the fluid layer is governed by the continuity and the NS equations as follows:

$$\nabla \cdot \mathbf{u} = 0, \tag{2.1}$$

$$\rho \left(\frac{\partial \mathbf{u}}{\partial t} + \mathbf{u} \cdot \nabla \mathbf{u} \right) = -\nabla p + \mu \nabla^2 \mathbf{u}, \tag{2.2}$$

where $\mathbf{u} = (u, v, w)$, p , ρ and μ denote velocity vector, pressure, density and viscosity, respectively. The operator ∇ is defined as $\nabla = (\partial/(\partial x), \partial/(\partial y), \partial/(\partial z))$.

Note that flow in a porous layer can also be governed by continuity and NS equations along with no-penetration and no-slip conditions at the fluid–solid interfaces. In general,

a porous medium's structure is either a sponge-like porous foam (e.g. metal-foam) or porous bed of packed particles (e.g. sand, gravel and aloxite). In the porous layer, several length scales are present: (i) average pore diameter (l_f); (ii) average particle diameter (l_s); and (iii) thickness of the porous layer (d_m). The first two are on a small scale, whereas the last is on a large scale. Due to the different length scales and complex boundary conditions, solving the boundary value problem governed by continuity and NS equations becomes very difficult. In this situation, the volume averaging method simplifies the issue by considering only the large-scale behaviour of the flow in the porous region (Tilton & Cortelezzi 2008). There are two types of volume averages: the superficial and intrinsic averages used in the volume averaging method. For a field variable ϕ_f in the fluid phase, the superficial and intrinsic averages are defined as

$$\langle \phi_f \rangle = \frac{1}{V} \int_{V_f} \phi_f \, dV_f, \tag{2.3}$$

and

$$\langle \phi_f \rangle^f = \frac{1}{V_f} \int_{V_f} \phi_f \, dV_f, \tag{2.4}$$

respectively, and they are related by $\langle \phi_f \rangle = \chi \langle \phi_f \rangle^f$, where χ is the porosity. Here, $V_f < V$ is the volume of fluid contained in the averaging volume, V and $V_f/V = \chi$. Following the convention of Whitaker (1996), i.e. for an incompressible viscous flow, the velocity vector has to satisfy solenoidal characteristics but not pressure, one can derive the following continuity and volume-averaged NS equations:

$$\nabla \cdot \langle \mathbf{u} \rangle = 0, \tag{2.5}$$

$$\begin{aligned} \rho \left[\frac{1}{\chi} \frac{\partial \langle \mathbf{u} \rangle}{\partial t} + \frac{1}{\chi^2} \langle \mathbf{u} \rangle \cdot \nabla \langle \mathbf{u} \rangle + \frac{c_F}{K^{1/2}} |\langle \mathbf{u} \rangle| \langle \mathbf{u} \rangle + \nabla \cdot \langle \hat{\mathbf{u}} \hat{\mathbf{u}} \rangle \right] \\ = -\nabla \langle p \rangle^f + \mu \nabla^2 \langle \mathbf{u} \rangle - \frac{\mu}{K} \langle \mathbf{u} \rangle, \end{aligned} \tag{2.6}$$

where $\langle \mathbf{u} \rangle$ is the superficial volume-averaged velocity, which is also called the Darcy velocity, $\langle p \rangle^f$ is the intrinsic volume-averaged pressure, c_F is the form drag coefficient and K is the permeability of the porous medium. In this equation, the Darcy term ($\mu \langle \mathbf{u} \rangle / K$) represents a volume-averaged viscous drag, the Brinkman term ($\mu \nabla^2 \langle \mathbf{u} \rangle$) represents a volume-averaged viscous diffusion, the Forchheimer term ($\rho c_F K^{-1/2} |\langle \mathbf{u} \rangle| \langle \mathbf{u} \rangle$) represents form-drag due to inertial effects and the advection term ($\rho \langle \mathbf{u} \rangle \cdot \nabla \langle \mathbf{u} \rangle / \chi^2$) represents another drag that arises from inertial effects.

It is important to mention that when the difference between the velocity of the fluid and the volume-averaged velocity of the fluid ($\langle \hat{\mathbf{u}} \rangle$) is negligible, the advection term in the NS equation generates the terms $\rho \langle \mathbf{u} \rangle \cdot \nabla \langle \mathbf{u} \rangle / \chi^2$ and $\rho c_F K^{-1/2} |\langle \mathbf{u} \rangle| \langle \mathbf{u} \rangle$ that are of order of $O(\rho |\langle \mathbf{u} \rangle|^2 / \chi^2 d_m)$ and $O(\rho c_F |\langle \mathbf{u} \rangle|^2 / l_f)$, respectively. This indicates that the contribution of advection term $\rho \langle \mathbf{u} \rangle \cdot \nabla \langle \mathbf{u} \rangle / \chi^2$ is negligible in comparison with the dominant Forchheimer term, $\rho c_F K^{-1/2} |\langle \mathbf{u} \rangle| \langle \mathbf{u} \rangle$. Note that the appropriate value of c_F for a given porous medium depends on experimental data. Due to insufficient experimental data, in practice, the inertia effects via form drag are generally dropped (Hill & Straughan 2009; Lasseux, Valdés-Parada & Bellet 2019). Furthermore, without a advection term, there is no mechanism for developing the flow field, which leads to a physically flawed and unrealistic situation (Vafai & Kim 1995). The present study concerns the flow

through porous materials whose permeability is relatively low, so the inertial effect is expected to be low. Accordingly, the flow in porous medium is modelled by the Darcy–Brinkman equation along with time derivative $((\rho/\chi)(\partial\mathbf{u}/\partial t))$ and advection term $(\rho\langle\mathbf{u}\rangle \cdot \nabla\langle\mathbf{u}\rangle/\chi^2)$. This model will be referred to as the DBA model from here onwards.

Furthermore, representing spatial volume-averaged velocity, $\langle\mathbf{u}\rangle$, and intrinsic volume-averaged pressure, $\langle p \rangle^f$, as \mathbf{u}_m and p_m , respectively, the governing equations in porous layer are transformed as follows:

$$\nabla \cdot \mathbf{u}_m = 0, \tag{2.7}$$

$$\frac{\rho}{\chi} \frac{\partial \mathbf{u}_m}{\partial t} + \frac{\rho}{\chi^2} \mathbf{u}_m \cdot \nabla \mathbf{u}_m = -\nabla p_m - \frac{\mu}{K} \mathbf{u}_m + \frac{\mu}{\chi} \nabla^2 \mathbf{u}_m, \tag{2.8}$$

where $\mathbf{u}_m = (u_m, v_m, w_m)$.

The dimensional no-slip and no-penetration conditions are considered at the upper and lower layers of the system, which are as follows:

$$u = U, \quad v = w = 0 \quad \text{at } z = d, \tag{2.9}$$

$$\mathbf{u}_m = 0 \quad \text{at } z = -d_m. \tag{2.10}$$

With respect to interface conditions, we assume the continuity conditions, i.e. continuity of velocity,

$$\mathbf{u} = \mathbf{u}_m \tag{2.11}$$

and normal stresses,

$$p - 2\mu \frac{\partial w}{\partial z} = p_m - \left(\frac{2\mu}{\chi} \right) \frac{\partial w_m}{\partial z}. \tag{2.12}$$

The continuity of velocity at the interface ensures mass conservation, preventing any unrealistic accumulation or depletion of mass. In addition, the forces exerted by the fluid and the porous medium on each other must be balanced. Further conditions related to tangential stresses must also be considered, which are given by the following equations:

$$\frac{\partial u}{\partial z} = \frac{1}{\chi} \frac{\partial u_m}{\partial z} - \frac{\beta}{\sqrt{K}} u_m, \quad \frac{\partial v}{\partial z} = \frac{1}{\chi} \frac{\partial v_m}{\partial z} - \frac{\beta}{\sqrt{K}} v_m, \tag{2.13a,b}$$

where β is the stress-jump coefficient Ochoa-Tapia & Whitaker (1995a). However, Hill & Straughan (2009) have utilised the generalisation of the condition of Jones (1973)

$$\frac{\partial u}{\partial z} + \frac{\partial w}{\partial x} = \frac{1}{\chi} \left(\frac{\partial u_m}{\partial z} + \frac{\partial w_m}{\partial x} \right) - \frac{\beta}{\sqrt{K}} u, \tag{2.14}$$

$$\frac{\partial v}{\partial z} + \frac{\partial w}{\partial y} = \frac{1}{\chi} \left(\frac{\partial v_m}{\partial z} + \frac{\partial w_m}{\partial y} \right) - \frac{\beta}{\sqrt{K}} v, \tag{2.15}$$

to include the shear stress at the interface, but in this study, we use the approach of Ochoa-Tapia & Whitaker (1995a), as it has shown better agreement with experimental observations. Furthermore, we have compared the effects of these two different interface conditions on the instability point and found that the results between the two remain largely consistent (table 7). A thorough and detailed discussion on the interface condition can be found in the work of Ochoa-Tapia & Whitaker (1995a,b).

To proceed with the linear stability analysis of the plane Couette flow, we non-dimensionalise the above governing equations (2.1)–(2.2) for fluid layer, (2.7)–(2.8) for porous layer, boundary conditions (2.9)–(2.10) and interface conditions (2.11)–(2.14). For the same, in the fluid layer, the lengths are non-dimensionalised by d , velocity components by U , time by d/U and pressure by $\mu U/d$. Thus, the non-dimensional governing equations for the fluid layer become

$$\nabla \cdot \mathbf{u} = 0, \tag{2.16}$$

$$Re \left(\frac{\partial \mathbf{u}}{\partial t} + \mathbf{u} \cdot \nabla \mathbf{u} \right) = -\nabla p + \nabla^2 \mathbf{u}. \tag{2.17}$$

Here, $Re = Ud/\nu$ is the Reynolds number, where ν represents the kinematic viscosity of the fluid.

For the porous layer, lengths are non-dimensionalised by d_m , velocity components by U_m , where U_m is the basic velocity component along the horizontal direction in the porous layer at $z_m = 0$, time by d_m/U_m and pressure by $\mu U_m/d_m$. Hence, the non-dimensional governing mass and momentum equations for the porous layer are

$$\nabla_m \cdot \mathbf{u}_m = 0, \tag{2.18}$$

$$\frac{Re_m}{\chi} \left(\frac{\partial \mathbf{u}_m}{\partial t_m} + \frac{1}{\chi} \mathbf{u}_m \cdot \nabla_m \mathbf{u}_m \right) = -\nabla_m p_m - \frac{1}{\delta^2} \mathbf{u}_m + \frac{1}{\chi} \nabla_m^2 \mathbf{u}_m, \tag{2.19}$$

where ∇_m is defined as $\nabla_m = (\partial/(\partial x_m), \partial/(\partial y_m), \partial/(\partial z_m))$. In the above equations, $\delta = \sqrt{K}/d_m$ is the Darcy number. The Reynolds number in the porous layer is defined as $Re_m = U_m d_m/\nu$.

The non-dimensional boundary conditions are as follows:

$$u = 1, \quad v = w = 0 \quad \text{at } z = 1, \tag{2.20}$$

$$\mathbf{u}_m = 0 \quad \text{at } z_m = -1. \tag{2.21}$$

At the interface of fluid and porous layers, i.e. at $z = 0 = z_m$:

$$Re \mathbf{u} = Re_m \hat{d} \mathbf{u}_m, \quad p - 2 \frac{\partial w}{\partial z} = \left(\frac{\hat{d}^2 Re_m}{Re} \right) p_m - \left(\frac{2 \hat{d}^2}{\chi} \right) \left(\frac{Re_m}{Re} \right) \frac{\partial w_m}{\partial z_m}, \tag{2.22}$$

$$\left(\frac{Re}{\hat{d}^2 Re_m} \right) \frac{\partial u}{\partial z} = \frac{1}{\chi} \frac{\partial u_m}{\partial z_m} - \frac{\beta}{\delta} u_m, \quad \left(\frac{Re}{\hat{d}^2 Re_m} \right) \frac{\partial v}{\partial z} = \frac{1}{\chi} \frac{\partial v_m}{\partial z_m} - \frac{\beta}{\delta} v_m, \tag{2.23}$$

where $\hat{d} = d/d_m$ is the depth ratio.

2.2. Basic state

We are interested in studying the linear stability analysis of the base flow to infinitesimal disturbances. For this, we assume that the flow is steady, unidirectional and

fully developed. The non-dimensional base flow in the fluid and porous layers is given by

$$\bar{U} = \frac{\hat{d}(1 + e^{2\sqrt{\chi}/\delta}) + \beta\sqrt{\chi}\hat{d}(1 - e^{2\sqrt{\chi}/\delta})}{\hat{d}(1 + e^{2\sqrt{\chi}/\delta}) - \delta\sqrt{\chi}(1 - e^{2\sqrt{\chi}/\delta}) + \beta\sqrt{\chi}\hat{d}(1 - e^{2\sqrt{\chi}/\delta})}z - \frac{\delta\sqrt{\chi}(1 - e^{2\sqrt{\chi}/\delta})}{\hat{d}(1 + e^{2\sqrt{\chi}/\delta}) - \delta\sqrt{\chi}(1 - e^{2\sqrt{\chi}/\delta}) + \beta\sqrt{\chi}\hat{d}(1 - e^{2\sqrt{\chi}/\delta})}, \quad (2.24)$$

$$\bar{V} = \bar{W} = 0, \quad (2.25)$$

and

$$\bar{U}_m = -\frac{e^{2\sqrt{\chi}/\delta}}{(1 - e^{2\sqrt{\chi}/\delta})}e^{(\sqrt{\chi}/\delta)z_m} + \frac{1}{(1 - e^{2\sqrt{\chi}/\delta})}e^{-(\sqrt{\chi}/\delta)z_m}, \quad \bar{V}_m = \bar{W}_m = 0, \quad (2.26)$$

respectively.

As can be seen from (2.24), the fluid velocity is linear in nature. In contrast to a Darcy porous layer (Chang *et al.* 2017), (2.26) gives the non-zero basic velocity, and the profile for the same is concave downwards. This might be the potential behind the instability of the plane Couette flow in the Darcy–Brinkman layer.

2.3. Perturbed state

The temporal linear stability analysis of the above base flow is performed by decomposing the flow variables into the base flow and infinitesimal perturbation as $q = \bar{Q} + q'$, where \bar{Q} and q' stand for the basic quantities and the perturbation quantities, respectively. The perturbed variables are considered in normal mode form as

$$q' = Q(z) \exp(iax + iby - i\sigma t), \quad (2.27)$$

$$q'_m = Q_m(z_m) \exp(ia_mx_m + ib_my - i\sigma_mt_m), \quad (2.28)$$

for both fluid and porous layers, respectively, with the relation $a = \hat{d}a_m$, $b = \hat{d}b_m$ and $\sigma = (Re_m\hat{d}^2/Re)\sigma_m$. Here, a and b are wavenumbers in x and y directions in the fluid layer, respectively, and a_m and b_m are the corresponding wavenumbers in the porous layer. In the present article, we have focused on the temporal linear stability analysis where wavenumbers are real, and wave speeds $\sigma = \sigma^r + i\sigma^i$ and $\sigma_m = \sigma_m^r + i\sigma_m^i$ are complex (Sengupta & De 2021; Zou *et al.* 2023). Depending on whether $\sigma^i < 0$, $\sigma^i = 0$, or $\sigma^i > 0$, the perturbations are categorised as stable, neutrally stable or unstable, respectively. Since it is observed that two-dimensional disturbances are least stable (see table 6 in Appendix A), it is sufficient to study the stability analysis of isothermal plane Couette flow by considering two-dimensional disturbances. Consequently, the spanwise components of wavenumber b and b_m are considered as zero.

After substituting (2.27)–(2.28) in (2.16)–(2.25) and neglecting the nonlinear terms in the resulting equations, the perturbed governing equations and boundary conditions are as

follows:

$$(D^2 - a^2 - ia Re \bar{U})(D^2 - a^2)W = -i\sigma Re(D^2 - a^2)W, \tag{2.29}$$

$$\begin{aligned} &\left(\frac{D_m^2 - a_m^2}{\chi} - \frac{1}{\delta^2}\right)(D_m^2 - a_m^2)W_m - \frac{ia_m Re_m}{\chi^2}(D_m^2 - a_m^2 - D_m^2 \bar{U}_m)W_m \\ &= -\frac{i\sigma_m Re_m}{\chi}(D_m^2 - a_m^2)W_m, \end{aligned} \tag{2.30}$$

$$W(1) = DW(1) = 0, \tag{2.31}$$

$$W_m(-1) = D_m W_m(-1) = 0, \tag{2.32}$$

$$Re W(0) = Re_m \hat{d} W_m(0), \quad Re DW(0) = Re_m \hat{d}^2 D_m W_m(0), \tag{2.33a,b}$$

$$\begin{aligned} &D^3 W(0) - ia Re \bar{U}(0)DW(0) + ia Re D\bar{U}(0)W(0) - 3a^2 DW + \left(\frac{\hat{d}^4 Re_m}{Re \delta^2}\right) D_m W_m(0) \\ &- \left(\frac{\hat{d}^4 Re_m}{\chi Re}\right) D_m^3 W_m(0) + \left(\frac{Re_m \hat{d}^4}{\chi Re}\right) a_m^2 D_m W_m(0) - \left(\frac{\hat{d}^4 Re_m^2}{\chi^2 Re}\right) ia_m \bar{U}_m D_m W_m \\ &+ \left(\frac{\hat{d}^4 Re_m^2}{\chi^2 Re}\right) ia_m D_m \bar{U}_m W_m = -i\sigma Re DW(0) + i\sigma_m \left(\frac{\hat{d}^4 Re_m^2}{\chi Re}\right) D_m W_m(0), \end{aligned} \tag{2.34}$$

$$\frac{Re}{\hat{d}^3} D^2 W(0) = \frac{Re_m}{\chi} D_m^2 W_m(0) - \frac{\beta}{\delta} Re_m D_m W_m(0), \tag{2.35}$$

where $D = d/dz$ and $D_m = d/dz_m$.

2.4. Kinetic energy budget

An immediate way to check whether the given flow can be unstable or not under linear theory is by looking at the sign of the rate of change of the disturbance kinetic energy (i.e. the sign of growth rate of kinetic energy). For the flow to be unstable, the rate of disturbance kinetic energy (δ_{KE}) of the system must change its sign from negative to positive. Thus, to check the instability of the isothermal plane Couette flow as well as the mechanism of instability, the help of the energy budget analysis is taken.

The kinetic energy balance equations are obtained by multiplying the disturbed velocity vector to both sides of the linear disturbance momentum equations and then integrating the equations over $([0, 1] \times [0, 2\pi/a])$ for fluid layer and $([-1, 0] \times [0, 2\pi/a_m])$ for porous layer (Boomkamp & Miesen 1996; Sharma, Aleria & Bera 2024). Combining the equations for fluid and porous layers, the kinetic energy balance equation takes the standard form:

$$\delta_{KE} = \frac{\partial(KE)}{\partial t} + \frac{\partial(KE_m)}{\partial t_m} = E_s + E_d + E_I + E_{d_m} + E_{D_m}. \tag{2.36}$$

In (2.36), the transfer of kinetic energy via Reynolds stress from or to the basic flow is represented by E_s , and energy dissipation via viscosity effects is represented by E_d

Material	Porosity χ	Pore size d_p [m]	Permeability K [m ²]	Darcy number $\delta_p = \sqrt{K}/d_p$
Aloxite 1	0.58	3.30×10^{-4}	6.45×10^{-10}	7.70×10^{-2}
Aloxite 2	0.52	6.86×10^{-4}	1.60×10^{-9}	5.83×10^{-2}
Foametal A	0.78	4.06×10^{-4}	9.68×10^{-9}	2.42×10^{-1}
Foametal B	0.78	8.64×10^{-4}	3.93×10^{-8}	2.29×10^{-1}
Foametal C	0.79	1.14×10^{-3}	8.20×10^{-8}	2.51×10^{-1}
Aluminium foam 1	0.92	2.50×10^{-3}	2.35×10^{-7}	1.93×10^{-1}
Aluminium foam 2	0.95	4.95×10^{-3}	2.48×10^{-7}	1.006×10^{-1}

Table 1. Geometrical characteristics of some porous materials (Paek *et al.* 2000; Goyeau *et al.* 2003; Kamath, Balaji & Venkateshan 2011).

and E_{d_m} for fluid and porous layer, respectively. The energy loss against surface drag is denoted by E_{D_m} . The disturbance kinetic energy due to work done by the perturbed stresses at the interface between the porous and fluid layers is represented by E_I . Here KE and KE_m denote the perturbed kinetic energy in the fluid and the porous layers, respectively. The expressions of each term in (2.36) are given in Appendix B. The Gauss–Chebyshev quadrature formula is used to compute the integrals in (2.36). The instability mechanism of the flow and the type of mode are determined by the kinetic energy balance equation. The contribution of E_d , E_{d_m} and E_{D_m} in the kinetic energy budget is used in this study to define the type of mode. If the contribution of E_d ($E_{d_m} + E_{D_m}$) is greater than 70 % in balancing the contribution of E_s , the instability is said to be dominated by fluid (porous) mode.

3. Numerical results and discussion

The Chebyshev spectral collocation method is used to solve the governing equations (2.29)–(2.30) and boundary conditions (2.31)–(2.35). Since, the Chebyshev polynomials are defined in $[-1, 1]$, the fluid layer $[0, 1]$ and porous layer $[-1, 0]$ are transformed into $[-1, 1]$ by using the transformation $\eta = 2z - 1$ and $\eta_m = -2z_m - 1$, respectively (Canuto *et al.* 1988; Anjali, Khan & Bera 2022). Thus, (2.29)–(2.30) together with boundary conditions (2.31)–(2.35) results in a generalised eigenvalue problem.

The flow is controlled by four parameters: depth ratio (\hat{d}), porosity (χ), Darcy number (δ) and stress-jump coefficient (β). In general, the porosity value for natural porous media is < 0.6 , where the Darcy model is normally used. However, for man-made porous media (e.g. metallic foam), the same may be close to 1, in which the non-Darcy model is preferred. A compilation of the porosity of some common porous materials is also given in table 1, in which the Darcy number (δ_p) is defined based on the pore size. In the present study, the Darcy number (δ) is defined based on the depth of the porous layer. The porous layer in our study primarily consists of either foametal A or foametal B. As mentioned in table 1, the Darcy number based on pore diameter (δ_p) for foametal A is 2.42×10^{-1} , where porous diameter is 4.06×10^{-4} m. Darcy number based on the depth of the porous layer (δ) can be given as $\delta = \delta_p \times d_p/d_m$. For example, when the thickness of the porous layer is 2.5 cm, δ will be approximately 0.004, whereas when the thickness is 1 cm, δ will be around 0.01. In the case of foametal B with a porous layer thickness of 1 cm, δ is estimated to be about 0.02. Similarly, for aluminum foam with a porous layer thickness of 0.5 cm, the value of δ will be approximately 0.1. Accordingly, δ is taken in the range $0.005 \leq \delta \leq 0.1$ and χ is fixed at 0.78 for most of the analysis. The selection of

N	σ^i	σ^r
30	-0.12848629	0.54461030
40	-0.12815094	0.54487819
50	-0.12816974	0.54486524
60	-0.12816926	0.54486506
70	-0.12816934	0.54486492
80	-0.12817038	0.54486537

Table 2. Convergence of the least-stable eigenvalue by Chebyshev spectral collocation method for $a = 2$, $Re = 500$, $\hat{d} = 0.12$, $\chi = 0.78$, $\delta = 0.009$ and $\beta = 0$.

\hat{d}	Re	σ^i	σ^r
3	1000	-0.06197180	0.24591209
	10 000	-0.02240795	0.10421233
	100 000	-0.00706574	0.08622590
5	1000	-0.06036383	0.24873108
	10 000	-0.03033481	0.11157825
	100 000	-0.00728164	0.05335407

Table 3. Eigenvalues with largest imaginary part for different values of \hat{d} at $a = 0.5$, $\chi = 0.78$, $\delta = 0.1$ and $\beta = 0$.

the range of the depth ratio is based on the fact that for $0.005 \leq \delta \leq 0.01$, the maximum value of \hat{d} for which the flow will be linearly unstable is found to be around 0.2, in fact for $\delta/\hat{d} < 10^{-1}/2$ the flow is linearly stable. To cover most of the range of δ , the upper limit of \hat{d} is fixed at 0.2. On the other hand, decreasing \hat{d} beyond 0.01, the flow characteristics remain almost the same on any further decrement of \hat{d} . Thus, the lower limit of \hat{d} is fixed at 0.01. Therefore, to understand the role of the location of interface on the stability of flow \hat{d} has been considered in the range $0.01 \leq \hat{d} \leq 0.2$. The effect of stress-jump coefficient on the same is emphasised by taking two different values of 0 and 0.7 of β (Ochoa-Tapia & Whitaker 1995b; Hill & Straughan 2009).

Before discussing the stability of the considered flow, the numerical code is verified in three different stages: first, the independence of solution on the order of polynomial; second, the comparison with existing results; and, third, whether the total rate of change of kinetic energy at the critical point is zero or not. The convergence of the numerical method is examined by varying the degree of Chebyshev polynomial, N , and is shown in table 2. It can be seen that $N = 70$ is sufficient to perform the numerical calculations. It is well known that plane Couette flow in a purely fluid channel is linearly stable (Romanov 1973; Orszag & Patera 1980). The similar characteristic is also observed for the present problem when the value of depth ratio is large (see table 3). For verifying our results with those of Chang *et al.* (2017), Darcy’s law is chosen to model the porous media instead of the present model, and the Beavers–Joseph condition is used at the fluid–porous interface. The comparison between present and existing results for $\chi = 0.3$, $\delta = 0.001$, $\alpha = 0.1$ (Beavers–Joseph constant) and $a = 1.0$ are listed in table 4 and a good agreement between the results is found. Finally, it has been checked that the total rate of change of kinetic energy at the critical point is zero (shown in the subsequent result section). All the above analyses support the verification of the present numerical code. To check

\hat{d}	Re	c_i (Chang <i>et al.</i> 2017)	c_i (present study)
0.5	10^4	-5.20861×10^{-2}	-5.21074×10^{-2}
	10^6	-2.31748×10^{-3}	-2.10192×10^{-3}
1.0	10^4	-5.25143×10^{-2}	-5.25325×10^{-2}
	10^6	-1.06924×10^{-2}	-1.06896×10^{-2}
10.0	10^4	-5.28401×10^{-2}	-5.28577×10^{-2}
	10^6	-1.07809×10^{-2}	-1.07802×10^{-2}

Table 4. The largest imaginary parts of the leading eigenvalues obtained by Chang *et al.* (2017) and present study for different values of \hat{d} and Re at $\chi = 0.3$, $\delta = 0.001$, $\alpha = 0.1$ and $a = 1.0$.

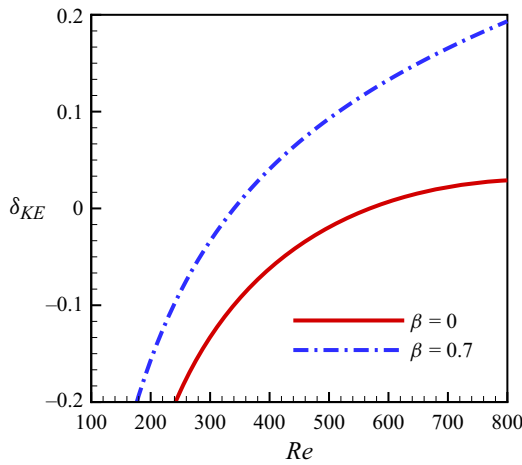


Figure 2. Growth rate of kinetic energy as a function of Re for $a = 0.5$, $\hat{d} = 0.1$, $\delta = 0.01$ and $\chi = 0.78$.

the possible existence of instability of the present problem, we have investigated whether the δ_{KE} will change its sign from negative to positive or not as a function of Reynolds number. It can be seen from figure 2 that the δ_{KE} changes its sign from negative to positive for $Re \in (100, 800)$, thus indicating that isothermal plane Couette flow in a superposed fluid–porous system will be unstable under the consideration of present model.

Figure 3(a,b) shows the neutral stability curve for different values of depth ratio at $\beta = 0$ and $\beta = 0.7$, respectively, wherein the neutral curve has either a single or dual lobe. From figure 3(a), for small values of depth ratio in the range $(0.01 \leq \hat{d} \leq 0.05)$, the neutral curve has a single lobe. As \hat{d} increases to 0.1, two lobes of the neutral stability curve appear and Re_c is observed in the left lobe. Whereas for $\hat{d} = 0.2$, Re_c shifts to the right lobe of the neutral stability curve. In the case of $\beta = 0.7$, single lobe of the neutral curve is obtained for all considered values of \hat{d} . Here, for increasing the value of the stress jump coefficient, Re_c decreases, which implies that the stress jump at the fluid–porous interface destabilises the flow. For both values of β , Re_c increases on increasing the depth of the fluid layer, i.e. \hat{d} stabilises the flow.

The value of different terms of the kinetic energy balance equation as a function of \hat{d} , at the critical point obtained from figure 3, are plotted in figure 4(a,b) for $\beta = 0$ and 0.7, respectively. It can be seen from figure 4(a), that the positive-definite term E_s is mainly

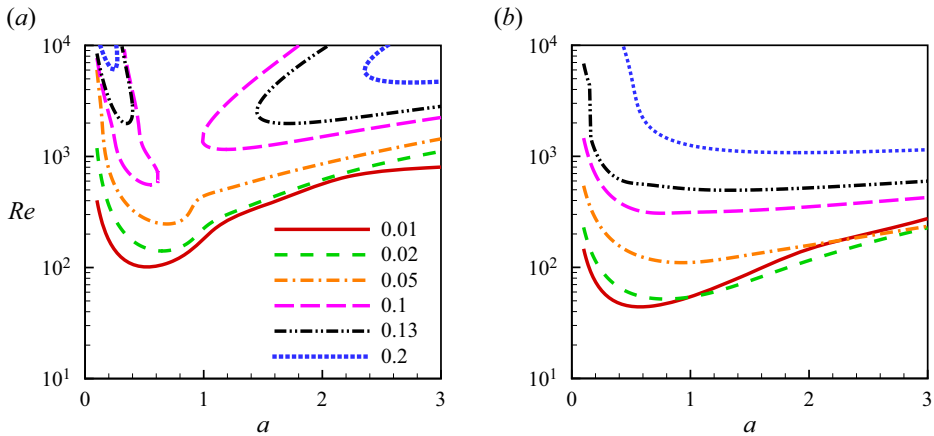


Figure 3. Neutral stability curves in (a, Re) plane for different values of \hat{d} at $\delta = 0.01$ and $\chi = 0.78$: (a) $\beta = 0$; (b) $\beta = 0.7$.

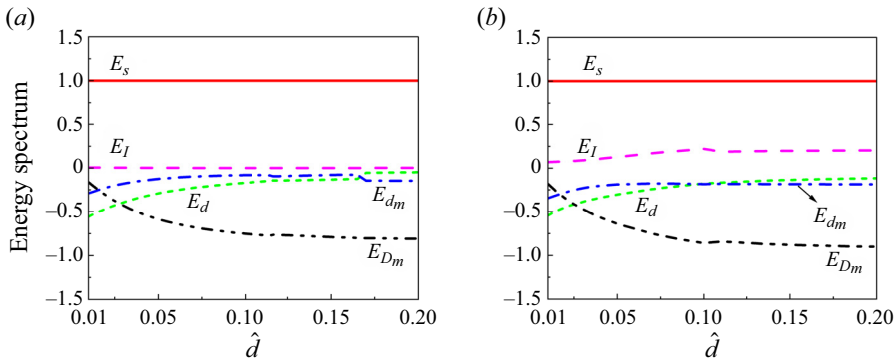


Figure 4. Different terms of kinetic energy balance as a function of \hat{d} at (a_c, Re_c) for $\delta = 0.01$ and $\chi = 0.78$: (a) $\beta = 0$; (b) $\beta = 0.7$.

balanced by E_{D_m} for $\hat{d} \geq 0.05$, whereas, for $\hat{d} < 0.05$, E_s is balanced by E_d , E_{d_m} and E_{D_m} . Along these lines, the mode of instability is defined as porous for $\hat{d} \geq 0.05$, and mixed for $\hat{d} < 0.05$. Similar characteristics can also be seen in figure 4(b). In this case, porous and mixed mode dominate the instability for $\hat{d} \geq 0.04$ and for $\hat{d} < 0.04$, respectively. It is important to mention here that in contrast to $\beta = 0$, here, the instability of flow is due to the combined effect of E_s and E_l . The destabilising nature of β in figure 3(b) is a consequence of the sizable contribution of E_l . Furthermore, a close look at figure 4(a) discloses that there exists a threshold value of $\hat{d} (\approx 0.165)$, beyond which the contribution of E_{D_m} suddenly decreases and corresponding E_{d_m} increases, which causes the shifting of Re_c from left to right lobe in figure 3(a).

As can be seen in the literature (Chang *et al.* 2017; Samanta 2020), the neutral curve displays a bimodal form and then a unimodal form as the depth ratio increases where the left lobe corresponds to the porous mode and the right lobe corresponds to the fluid mode. In the present study, two lobes for $\hat{d} \geq 0.1$ are obtained, and both lobes correspond to porous mode only. Here, the porous mode also becomes more stable for increasing values of \hat{d} .

Isothermal plane Couette flow over a porous layer

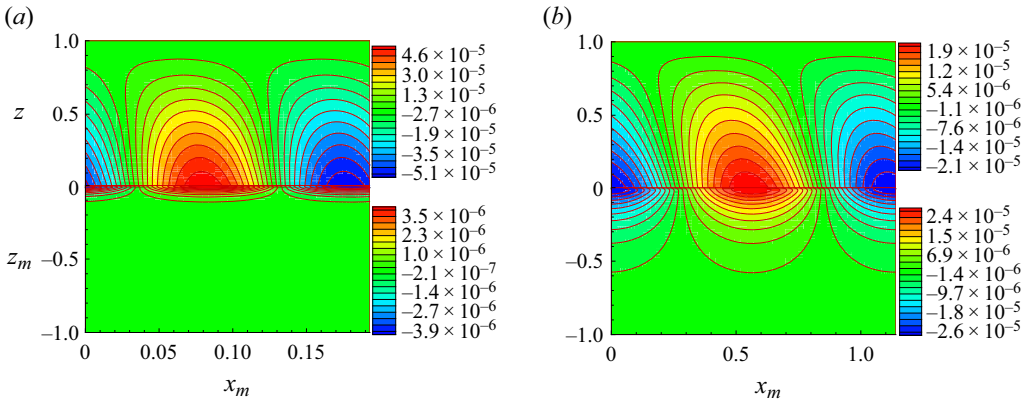


Figure 5. The streamfunction pattern at $\delta = 0.01$, $\chi = 0.78$ and $\beta = 0$: (a) $(a_c, Re_c) = (0.651, 140.913)$, $\hat{d} = 0.02$; (b) $(a_c, Re_c) = (0.551, 556.605)$, $\hat{d} = 0.1$.

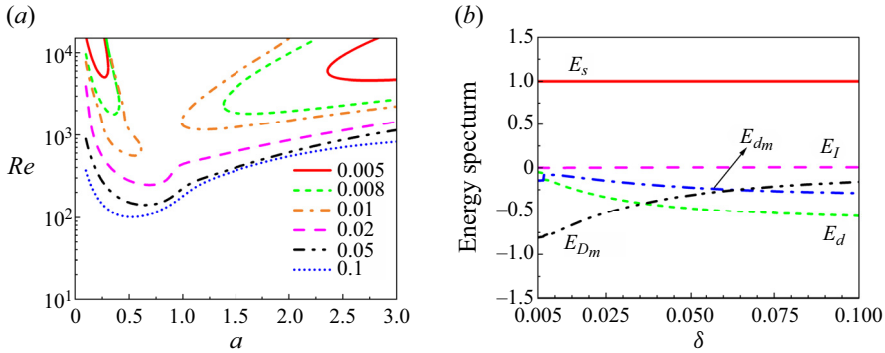


Figure 6. (a) Neutral stability curves for different values of δ and (b) energy components as a function of δ at $\hat{d} = 0.1$, $\chi = 0.78$ and $\beta = 0$.

The pattern of streamfunction at the critical states for $\hat{d} = 0.02$ and 0.1 , obtained from figure 3(a), are shown in figure 5(a,b), respectively, which allows for a deeper examination of the primary instability mode and aids in visualising the flow dynamics. The fluid layer extension from 0 to 1 and the porous layer extension from -1 to 0 are represented by the vertical axis. The critical wavelength, which is scaled by \hat{d} for the porous layer, is depicted on the horizontal axis. As we can see, streamfunction patterns occupy both layers, however for $\hat{d} = 0.1$, the penetration in porous layer is more in comparison with the same for $\hat{d} = 0.02$, thus representing the porous and mixed mode, respectively. These findings support the results obtained from the energy budget analysis.

In order to understand the role of media permeability on the instability mechanism, the neutral stability curve in the (a, Re) -plane for different values of Darcy number and the corresponding energy budget spectrum at critical points are displayed in figure 6(a,b), respectively. It is observed that at $\delta = 0.005$, the neutral stability curve has two lobes, both correspond to porous mode, and the critical value is obtained at $(2.741, 4634.666)$. The characteristic of the neutral stability curve remains the same for $\delta = 0.008$ and 0.01 , but Re_c decreases to 1794.759 and 556.605, respectively. On further increasing the value of δ , the neutral stability curve with a single lobe is observed. Similar to figure 4, figure 6(b) also displays porous and mixed mode for $\delta \leq 0.02$ and $\delta > 0.02$, respectively. In addition, also similar to figure 4, a jump in E_{d_m} and E_{D_m} can be seen at $\delta \approx 0.007$, which causes the

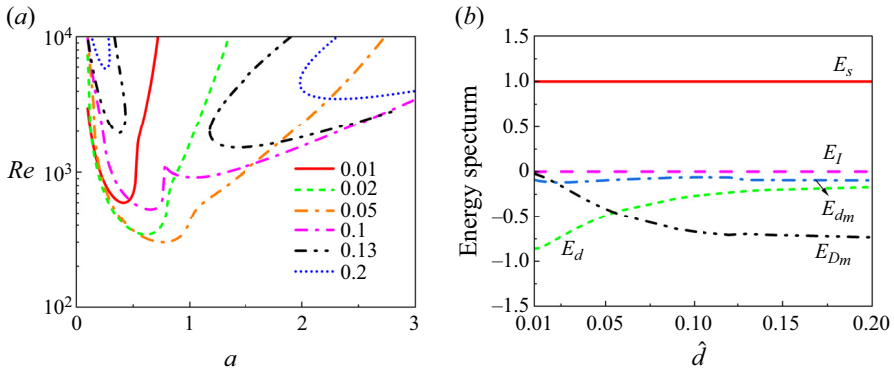


Figure 7. (a) Neutral stability curves for different values of \hat{d} ; (b) energy components as a function of \hat{d} eliminating advection term at $\delta = 0.01$, $\chi = 0.78$ and $\beta = 0$.

shift in Re_c from right to left lobe of neutral stability curve in figure 6(a). As mentioned in Chang *et al.* (2006), wherein the Darcy model is considered, an increase in δ causes the system to become more unstable. In the present study, the similar characteristic is observed for the considered range of δ .

Now, we are curious to know whether the instability of Couette flow can be seen or not when the inertial effect in terms of advection term is ignored in the considered model (from here onwards, called the DB model). If it appears, how does the advection term influence the instability mechanism? A comparative study between DB and DBA models is required. To do so, we have eliminated the advection term $(1/\chi^2)(\mathbf{u}_m \cdot \nabla_m)\mathbf{u}_m$ in the momentum equation (2.19) and a thorough analysis in terms of \hat{d} , χ and δ is made. Figure 7(a) represents the neutral stability curves for different values of \hat{d} and 7(b) displays the energy budget spectrum as a function of \hat{d} at critical point. Here, the values of all other parameters are kept the same as in figure 3(a). Similar to the DBA model, two lobes of neutral stability curve for $\hat{d} = 0.1, 0.13$ and 0.2 are observed, and the least-stable Re moves from the left to right lobe on increasing the value of \hat{d} . The critical value, Re_c , appears in the right lobe for $\hat{d} = 0.13$ and 0.2 . Furthermore, in contrast to the DBA model, for $\hat{d} = 0.1$, the instability is observed for the entire range of a . Interestingly, as \hat{d} is increased from 0.01 to 0.05 , the critical value of Re decreases, i.e. increasing fluid layer thickness destabilises the flow. However, further increasing of \hat{d} causes the flow to be more stable, i.e. Re_c increases as \hat{d} increases within the range, $0.05 \leq \hat{d} \leq 0.2$. Thus, the stabilising nature of \hat{d} , under the DBA model, is not strictly followed when the advective term is dropped in the momentum equation (see table 5). From figure 7(b), the transfer of kinetic energy via Reynolds stress to the basic flow in fluid and porous layers (i.e. E_s) is primarily balanced by E_d (E_{Dm}) when $\hat{d} < 0.055$ ($\hat{d} > 0.055$). However, in the vicinity of $\hat{d} = 0.055$, both E_d and E_{Dm} contribute equally. These result in fluid, porous and mixed modes for $\hat{d} < 0.055$, $\hat{d} > 0.055$ and in the neighbourhood of 0.055 , respectively. Note that in the range of \hat{d} where the fluid mode prevails, the destabilising nature of \hat{d} can be seen.

The streamfunction patterns at the critical point for $\hat{d} = 0.01, 0.055$ and 0.2 are shown in figure 8(a–c), respectively. It can be pointed out that, in the fluid mode, the patterns are primarily confined to the fluid layer. In the mixed mode, the patterns extend into both layers, but the penetration into the porous layer is minimal. In contrast, the porous mode exhibits patterns distributed almost equally between both layers.

\hat{d}	Re_c (DB)	Re_c (DBA)
0.01	599.361	101.216
0.02	341.804	140.913
0.05	300.316	246.680
0.10	534.743	556.605
0.13	1519.994	1980.078
0.20	3515.223	4633.445

Table 5. The value of critical Reynolds number for different values of \hat{d} at $\delta = 0.01$, $\chi = 0.78$ and $\beta = 0$.

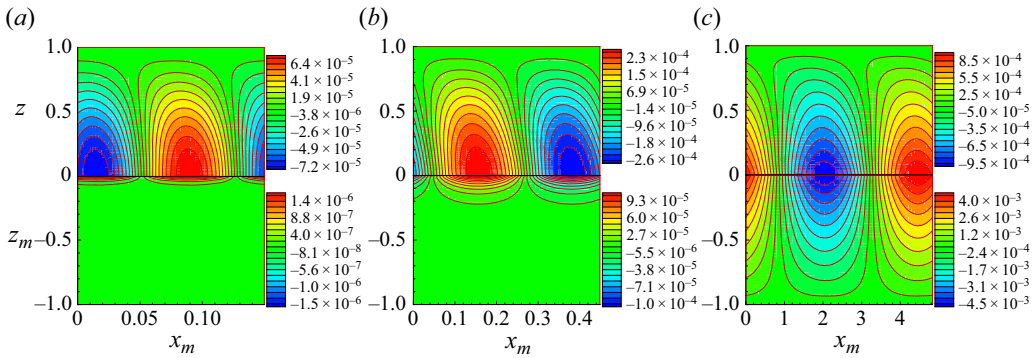


Figure 8. The streamfunction pattern at $\delta = 0.01$, $\chi = 0.78$ and $\beta = 0$: (a) $(a_c, Re_c) = (0.42, 599.361)$, $\hat{d} = 0.01$; (b) $(a_c, Re_c) = (0.77, 310.850)$, $\hat{d} = 0.055$; and (c) $(a_c, Re_c) = (2.33, 3515.223)$, $\hat{d} = 0.2$.

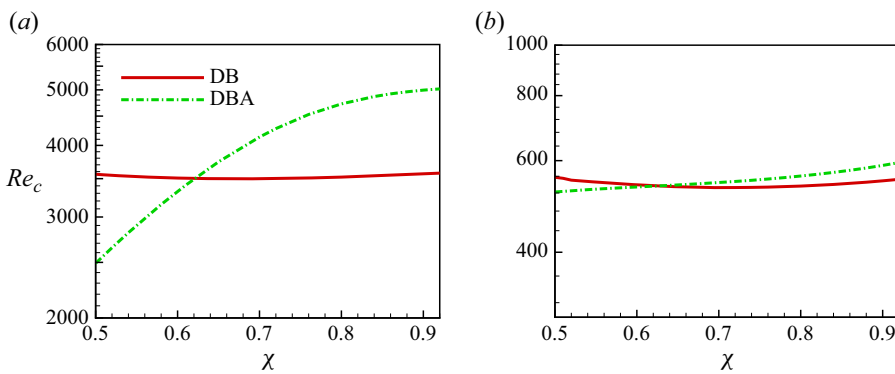


Figure 9. Variation of Re_c as a function of χ for $\hat{d} = 0.1$ and $\beta = 0$: (a) $\delta = 0.005$ and (b) $\delta = 0.01$.

The effect of the advection term on flow instability for different porosity and permeability is analysed in figure 9. A comparative study on instability boundary in the (χ, Re_c) -plane for DB as well as DBA models at $\delta = 0.005$ and 0.01 is made in figure 9(a,b), respectively. In contrast to a negligible change in Re_c as a function of χ for $\delta = 0.01$, a significant change in the same at $\delta = 0.005$ under the consideration of the DBA model is observed. In addition, the change in Re_c as a function χ under the DB model is negligible. For both values of δ , the flow becomes more (less) unstable under the DB model for $\chi > 0.62$ (< 0.62). It is also seen that porosity stabilises the flow under the DBA model but under the DB model it first destabilises and then stabilises the flow. As we have already seen, increasing media permeability (depth ratio) destabilises (stabilises) the

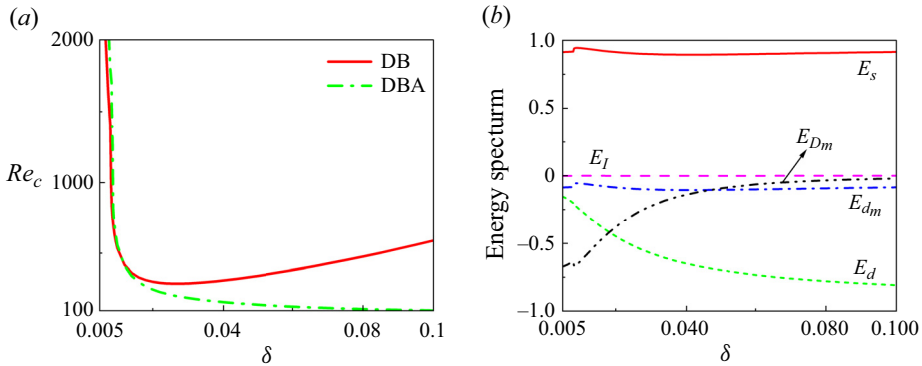


Figure 10. (a) Variation of Re_c and (b) energy components (DB model) as a function of δ at $\hat{d} = 0.1$, $\chi = 0.78$ and $\beta = 0$.

flow under the DBA model, but the influence of \hat{d} on the flow stability under the DB model is not straightforward. A natural question that arises is whether the influence of δ under the DB model will remain straightforward or not. To shed more light in this direction, variation of Re_c as a function δ is analysed in figure 10. It reveals that, for the DBA model, the critical Reynolds number (Re_c) decreases as the parameter δ increases. In contrast, when considering the DB model, Re_c initially decreases with increasing δ , followed by an increase as δ increases, which may be the consequence of mode change from porous to fluid.

It is worth mentioning here that the above theoretical prediction can be helpful in different engineering applications wherever Couette flow in a fluid overlying porous medium is encountered, specifically, the movement of ships in a port or shallow ocean. For example, the ship’s propeller-induced flow mimics a scenario of Couette flow in fluid overlying a sedimented porous bottom (Kadir *et al.* 2024). To avoid damage to the aquatic ecosystem and sediment erosion, the ship’s operator has to know the ship’s appropriate maximum velocity, depth of water and nature of the seabed, i.e. quality of permeable sea bed, so that the fluid layers at the fluid–porous interface do not mix, i.e. the flow remains stable and smooth. This information will further optimise the pressure gradient at sediment and, thus, will help in preventing the erosion of sediment.

4. Conclusion

The current study examines the instability of isothermal Couette flow through a superposed fluid–porous system. The flow in the fluid layer is governed by the NS equation, whereas, in the porous layer, it is governed by the volume-averaged NS equation. Two situations have been considered: first, considering the inertial effect due to the advection term; and, second, ignoring the inertial effect due to the advection term. Using the Chebyshev spectral collocation method, the Orr–Sommerfeld eigenvalue problem is solved numerically. Even though it is known that the plane Couette flow in fluid overlying Darcy porous layer is always stable, its unstable behaviour is found for both the situations mentioned above. Three different modes are identified on the basis of the energy budget spectrum, and they are named as porous, fluid and mixed modes.

For the DBA model, the mode of instability changes at $\hat{d} \approx 0.05$ and $\delta \approx 0.02$ when $\beta = 0$. A single lobe of the neutral curve corresponding to mixed mode is observed for $\delta = 0.01$ and $0.01 \leq \hat{d} \leq 0.05$. On further increasing the value of \hat{d} , two lobes of the neutral

\hat{d}	b	Re_c
0.02	0.0	140.918
	0.1	142.608
	0.3	157.203
0.13	0.0	1980.200
	0.1	2065.627
	0.3	3353.320

Table 6. The values of Re_c for different values of b at $\chi = 0.78$, $\delta = 0.01$ and $\beta = 0$.

stability curve are seen and both lead to porous mode. It has been also noted that the critical value of Re shifts from left to right lobe on increasing (decreasing) values of \hat{d} (δ). In this situation, a sudden increase of the contribution of E_{d_m} and decrease of the same on E_d in the energy balance are seen. The stress-jump coefficient changes instability characteristic significantly and reduces the critical value of Re via energy production through stresses and velocities at the interface. Similar to plane Poiseuille flow (Deepu, Anand & Basu 2015), decreasing \hat{d} (increasing δ) increases the instability of the flow.

It has been found that in contrast to the DB model, for a relatively low permeable porous layer the critical value of Re changes significantly as a function of χ under the DBA model. However, there exists a threshold value of 0.62 of χ at which the instability boundary under both models remains the same. Beyond this threshold value, the inertial effect delays the onset of instability. Furthermore, whenever the fluid mode of instability is encountered in a certain range of \hat{d} (δ) under the DB model, the respective parameter acts as a destabilising (stabilising) factor.

Due to the lack of experimental work in this direction, the findings from the present study will also act as a stepping stone for experimentalists working in this direction. Furthermore, to have a deeper understanding of the flow mechanics that includes transitions to turbulence, a nonlinear stability analysis via cubic Landau theory (Sharma, Khandelwal & Bera 2018; Aleria, Khan & Bera 2024) or direct numerical simulations is required. These works are left for future study.

Acknowledgements. One of the authors, P.B. dedicates this work to Prof. K. Muralidhar, Indian Institute of Technology Kanpur, India, on his 66th birth anniversary. N.B. expresses gratitude to the Ministry of Human Resource Development (MHRD), India for providing financial support during, and the National Supercomputing Mission (NSM) for providing computing resources on ‘PARAM Ganga’ at IIT Roorkee. The authors acknowledge Mr Ajay Sharma, PhD Scholar, IIT Roorkee, for his valuable suggestion.

Declaration of interests. The authors report no conflict of interest.

Author ORCIDs.

- N. Barman <https://orcid.org/0000-0002-0355-1268>;
- A. Aleria <https://orcid.org/0000-0002-7802-6855>;
- P. Bera <https://orcid.org/0000-0002-9030-984X>.

Appendix A. Least-stable mode

Considering three-dimensional perturbation, [table 6](#) indicates that the least-stable mode is always two-dimensional.

\hat{d}	Re_c (Ochoa-Tapia & Whitaker 1995a)	Re_c (Jones 1973; Hill & Straughan 2009)
0.01	101.216	100.289
0.02	140.913	140.408
0.05	246.680	247.878
0.10	556.605	558.753
0.13	1980.078	1980.620
0.20	4633.445	4746.314

Table 7. The value of critical Reynolds number for different values of \hat{d} at $\delta = 0.01$, $\chi = 0.78$ and $\beta = 0$.

Appendix B. Expressions in the kinetic energy balance

The expressions in the kinetic energy balance are as follows:

$$KE = \frac{1}{2\lambda} \int_0^1 \int_0^\lambda (u'^2 + w'^2) dx dz, \tag{B1}$$

$$KE_m = \frac{1}{2\lambda_m \chi} \int_{-1}^0 \int_0^{\lambda_m} (u'_m{}^2 + w'_m{}^2) dx_m dz_m, \tag{B2}$$

$$E_s = -\frac{1}{\lambda} \int_0^1 \int_0^\lambda u' w' \left(\frac{d\bar{U}}{dz} \right) dx dz - \frac{1}{\lambda_m \chi^2} \int_{-1}^0 \int_0^{\lambda_m} u'_m w'_m \left(\frac{d\bar{U}_m}{dz_m} \right) dx_m dz_m, \tag{B3}$$

$$E_d = -\frac{1}{\lambda Re} \int_0^1 \int_0^\lambda \left[\left(\frac{\partial u'}{\partial x} \right)^2 + \left(\frac{\partial u'}{\partial z} \right)^2 + \left(\frac{\partial w'}{\partial x} \right)^2 + \left(\frac{\partial w'}{\partial z} \right)^2 \right] dx dz, \tag{B4}$$

$$E_{d_m} = -\frac{1}{\lambda_m Re_m \delta^2} \int_{-1}^0 \int_0^{\lambda_m} \left[\left(\frac{\partial u'_m}{\partial x_m} \right)^2 + \left(\frac{\partial u'_m}{\partial z_m} \right)^2 + \left(\frac{\partial w'_m}{\partial x_m} \right)^2 + \left(\frac{\partial w'_m}{\partial z_m} \right)^2 \right] dx_m dz_m, \tag{B5}$$

$$E_{D_m} = -\frac{1}{\lambda_m Re_m \delta^2} \int_{-1}^0 \int_0^{\lambda_m} (u'_m{}^2 + w'_m{}^2) dx_m dz_m, \tag{B6}$$

$$E_I = \frac{1}{\lambda Re} \int_0^1 \left[w' p' - \left(u' \frac{\partial u'}{\partial z} + w' \frac{\partial w'}{\partial z} \right) \right]_{z=0} dx - \frac{1}{\lambda_m Re_m \chi} \int_{-1}^0 \left[\chi w'_m p'_m - \left(u'_m \frac{\partial u'_m}{\partial z_m} + w'_m \frac{\partial w'_m}{\partial z_m} \right) \right]_{z_m=0} dx_m, \tag{B7}$$

where $\lambda = 2\pi/a$ and $\lambda_m = 2\pi/a_m$.

Appendix C. Comparison of stress conditions at the interface

In this Appendix, we present a comparison of the results obtained using two different tangential stress conditions at the interface of a two-layer system: one suggested by Ochoa-Tapia & Whitaker (1995a) and the other being the generalised Jones condition (Jones 1973). Table 7 summarises the critical Reynolds numbers for different values of \hat{d} .

REFERENCES

- ALERIA, A., KHAN, A. & BERA, P. 2024 Finite amplitude analysis of poiseuille flow in fluid overlying porous domain. *SIAM J. Appl. Maths* **84** (2), 433–463.
- ALLEN, M.B. 1984 *Collocation Techniques for Modelling Compositional Flows in Oil Reservoirs*. Springer.
- ANJALI, KHAN, A. & BERA, P. 2022 Stability of non-isothermal Poiseuille flow in a fluid overlying an anisotropic and inhomogeneous porous domain. *J. Fluid Mech.* **949**, A44.
- BARMAN, N., ALERIA, A. & BERA, P. 2024 Non-isothermal plane Couette flow and its stability in an anisotropic and inhomogeneous porous layer underlying a fluid layer saturated by water. *J. Heat Transfer* **146** (7), 072701.
- BLEST, D.C., DUFFY, B.R., MCKEE, S. & ZULKIFLE, A.K. 1999 Curing simulation of thermoset composites. *Compos. A: Appl. Sci. Manuf.* **30**, 1289–1309.
- BOOMKAMP, P.A.M. & MIESEN, R.H.M. 1996 Classification of instabilities in parallel two-phase flow. *Intl J. Multiphase Flow* **22**, 67–88.
- CANUTO, C., HUSSAINI, M.Y., QUARTERONI, A. & ZANG, T.A. 1988 *Spectral Method in Fluid Dynamics*. Springer.
- CHANG, M.H. 2005 Thermal convection in superposed fluid and porous layers subjected to a horizontal plane Couette flow. *Phys. Fluids* **17** (6), 064106.
- CHANG, M.H., CHEN, F. & STRAUGHAN, B. 2006 Instability of Poiseuille flow in a fluid overlying a porous layer. *J. Fluid Mech.* **564**, 287–303.
- CHANG, T.Y., CHEN, F. & CHANG, M.H. 2017 Stability of plane Poiseuille–Couette flow in a fluid layer overlying a porous layer. *J. Fluid Mech.* **826**, 376–395.
- DAVEY, A. 1973 On the stability of plane Couette flow to infinitesimal disturbances. *J. Fluid Mech.* **57** (2), 369–380.
- DEEPU, P., ANAND, S. & BASU, S. 2015 Stability of Poiseuille flow in a fluid overlying an anisotropic and inhomogeneous porous layer. *Phys. Rev. E* **92** (2), 023009.
- EWINGS, R.E. & WEEKES, S. 1998 Numerical methods for contaminant transport in porous media. *Comput. Math.* **202**, 75–95.
- GOURLAY, T. 2006 Flow beneath a ship at small underkeel clearance. *J. Ship Res.* **50** (3), 250–258.
- GOYEAU, B., LHUILLIER, D., GOBIN, D. & VELARDE, M.G. 2003 Momentum transport at a fluid–porous interface. *Intl J. Heat Mass Transfer* **46** (21), 4071–4081.
- HILL, A.A. & STRAUGHAN, B. 2009 Poiseuille flow in a fluid overlying a highly porous material. *Adv. Water Resour.* **32** (11), 1609–1614.
- JONES, I.P. 1973 Low Reynolds number flow past a porous spherical shell. *Proc. Camb. Phil. Soc.* **73** (1), 231–238.
- KADIR, A., *et al.* 2024 Ship propeller rotation threshold to prevent erosion and sedimentation in coastal waters. *J. Mar. Sci. Engng* 1–14.
- KAMATH, P.M., BALAJI, C. & VENKATESHAN, S.P. 2011 Experimental investigation of flow assisted mixed convection in high porosity foams in vertical channels. *Intl J. Heat Mass Transfer* **54** (25–26), 5231–5241.
- LASSEUX, D., VALDÉS-PARADA, F.J. & BELLET, F. 2019 Macroscopic model for unsteady flow in porous media. *J. Fluid Mech.* **862**, 283–311.
- LEE, K.C. & FINLAYSON, B.A. 1986 Stability of plane Poiseuille and Couette flow of a maxwell fluid. *J. Non-Newtonian Fluid Mech.* **21** (1), 65–78.
- MUKHERJEE, S. & GIRIBABU, D. 2021 Stability of plane Couette flow past an initially stressed solid. *Intl J. Engng Sci.* **169**, 103572.
- NIELD, D.A. 2003 The stability of flow in a channel or duct occupied by a porous medium. *J. Heat Transfer* **46** (22), 4351–4354.
- OCHOA-TAPIA, J. & WHITAKER, S. 1995a Momentum transfer at the boundary between a porous medium and a homogeneous fluid – I. Theoretical development. *Intl J. Heat Mass Transfer* **38** (14), 2635–2646.
- OCHOA-TAPIA, J. & WHITAKER, S. 1995b Momentum transfer at the boundary between a porous medium and a homogeneous fluid – II. Comparison with experiment. *Intl J. Heat Mass Transfer* **38** (14), 2647–2655.
- ORSZAG, S.A. & PATERA, A.T. 1980 Subcritical transition to turbulence in plane channel flows. *Phys. Rev. Lett.* **45** (12), 989.
- PAEK, J.W., KANG, B.H., KIM, S.Y. & HYUN, J.M. 2000 Effective thermal conductivity and permeability of aluminum foam materials. *Intl J. Thermophys.* **21**, 453–464.
- RAYLEIGH, L. 1914 LXII. Further remarks on the stability of viscous fluid motion. *Phil. Mag.* **28** (166), 609–619.
- ROMANOV, V.A. 1973 Stability of plane-parallel Couette flow. *Funct. Anal. Applics.* **7** (2), 137–146.
- SAMANTA, A. 2020 Linear stability of a plane Couette–Poiseuille flow overlying a porous layer. *Intl J. Multiphase Flow* **123**, 103160.

- SENGUPTA, S. & DE, S. 2019 Stability of Poiseuille flow of a Bingham fluid overlying an anisotropic and inhomogeneous porous layer. *J. Fluid Mech.* **874**, 573–605.
- SENGUPTA, S. & DE, S. 2020 Effect of Couette component on the stability of Poiseuille flow of a Bingham fluid–porous system: modal and non-modal approaches. *Phys. Fluids* **32** (6), 064103.
- SENGUPTA, S. & DE, S. 2021 Long-time instability and transient behavior of pressure-driven flow of a power-law fluid in a plane channel overlying a porous layer. *Phys. Fluids* **33** (5), 054109.
- SHANKAR, B.M., SHIVAKUMARA, I.S. & KUMAR, J. 2020 Benchmark solution for the hydrodynamic stability of plane porous-Couette flow. *Phys. Fluids* **32** (10), 104104.
- SHARMA, A., ALERIA, A. & BERA, P. 2024 Stability analysis of Poiseuille flow in an annulus partially filled with porous medium. *Phys. Fluids* **36** (2), 024104.
- SHARMA, A.K., KHANDELWAL, M.K. & BERA, P. 2018 Finite amplitude analysis of non-isothermal parallel flow in a vertical channel filled with a highly permeable porous medium. *J. Fluid Mech.* **857**, 469–507.
- TILLMARK, N. & ALFREDSSON, P.H. 1992 Experiments on transition in plane Couette flow. *J. Fluid Mech.* **235**, 89–102.
- TILTON, N. & CORTELEZZI, L. 2008 Linear stability analysis of pressure-driven flows in channels with porous walls. *J. Fluid Mech.* **604**, 411–445.
- VAFAI, K. & KIM, S. 1995 On the limitations of the Brinkman-Forchheimer-extended Darcy equation. *Intl J. Heat Fluid Flow* **16** (1), 11–15.
- WANG, X., OLSEN, S.M., MARTINEZ, A.E., OLSEN, K.N. & KIIL, S. 2018 Drag resistance of ship hulls: effects of surface roughness of newly applied fouling control coatings, coating water absorption, and welding seams. *J. Coat. Technol. Res.* **15**, 657–669.
- WHITAKER, S. 1996 The Forchheimer equation: a theoretical development. *Transp. Porous Media* **25** (1), 27–61.
- ZOU, S., BI, L., ZHONG, C., YUAN, X. & TANG, Z. 2023 A novel linear stability analysis method for plane Couette flow considering rarefaction effects. *J. Fluid Mech.* **963**, A33.